Experimental and Numerical Investigation of a Counter-Current Flow Bubble Column

Khan, H.; Kováts, P.; Zähringer, K.; Rzehak, R.;

Originally published:

December 2023

Chemical Engineering Science 285(2023), 119503

DOI: https://doi.org/10.1016/j.ces.2023.119503

Perma-Link to Publication Repository of HZDR:

https://www.hzdr.de/publications/Publ-36918

Experimental and Numerical Investigation of a Counter-Current Flow Bubble Column

Haris Khan[1*], Péter Kováts[2], Katharina Zähringer[2], Roland Rzehak[1]

[1]Helmholtz-Zentrum Dresden – Rossendorf, Institute of Fluid Dynamics, Bautzner Landstrasse 400, D-01328 Dresden, Germany

[2]Laboratory of Fluid Dynamics and Technical Flows, Otto-von-Guericke-Universität Magdeburg, Universitätsplatz 2, D-39106 Magdeburg, Germany

Abstract

Bubble columns are gas-liquid contactors that are used in many process-engineering applications. A counter-current liquid flow is frequently imposed to adjust the bubbles' residence-time and thus optimize mixing and mass-transfer. The present work describes measurements in such a device together with corresponding computational fluid dynamics simulations based on the Eulerian two-fluid framework. Bubble-size and -velocity are measured by shadow-imaging for a large range of gas and counter-current liquid flow rates, as well as different nozzle sizes. The corresponding liquid flow-fields are characterized by Particle Image Velocimetry. From the large experimental database, a few cases are selected to analyze the flow structure and effects of the bubble-size. In the simulations, different models for the drag- and lift-force acting on the bubbles are evaluated. While good agreement between experiments and simulations could be achieved for the gas-fraction and gas-velocity, differences are found for the liquid-velocity, which is generally overestimated in the calculations.

Keywords: countercurrent flow bubble column, shadowgraphy, PIV, Euler-Euler two-fluid model, CFD simulation

[*] Corresponding author. Email: h.khan@hzdr.de

TABLE OF CONTENTS

1 INTRODUCTION

Bubble columns are gas liquid contactors that are used in many process engineering applications. The wide range of applications includes e.g. absorption, catalytic slurry reactions, coal liquefaction, bioreactions (Shah et al 1982). Therein, a counter-current liquid flow is frequently imposed to adjust the bubbles' residence time and thus optimize mixing and mass transfer (Kraume 2012, Schlüter et al 2021). Despite its simple construction, the flow inside a bubble column is quite complex and a detailed understanding is still lacking to date, even if only the fluid dynamics is considered and additional phenomena such as mass transfer and chemical reactions (Khan et al 2023, Long et al. 2022, Hlawitschka et al. 2017) are excluded.

In this situation, multiphase computational fluid dynamics (CFD) is an increasingly recognized tool to complement experimental investigations (e.g. Joshi and Nandakumar 2015, Werner et al. 2014, Wu 2013, Laleh et al. 2012). Such simulations are made feasible by the Eulerian two-fluid framework, in which effects that appear on the scale of individual bubbles or small groups of bubbles are modeled, and only the large-scale flow on the scale of the entire column is resolved. However, despite some progress in recent years, the quest for accurate and broadly applicable closure models for the small-scale effects remains ongoing (Colombo et al 2021, Mühlbauer et al. 2019, Besagni et al. 2018).

While a number of recent rather comprehensive experimental studies considering bubble swarms rising in quiescent liquid (e.g. Kováts et al. 2020, Lucas and Ziegenhein 2019, Tyagi and Buwa 2017, Azizi et al 2017, Besagni et al. 2016, Wanke et al. 2015 Sathe et al. 2013) are available, counterflow bubble columns have only seldom been a subject of experimental measurements (Besagni 2021, Krepper et al. 2016, Colin et al. 2012). In the few available studies involving liquid counterflow, the bubbles were injected approximately uniformly over the column cross section, which imposes difficulties for optical measurement techniques. Therefore, in the present study a sparger consisting of seven nozzles arranged in a line is applied, which facilitates recording data in a plane spanned by this line and the vertical direction by optical methods. This flow configuration provides an interesting new test case for comparison with numerical simulations.

Position, size and velocity of the bubbles are measured by shadow imaging combined with Particle Tracking Velocimetry (PTV). The corresponding liquid flow fields in the column are characterized by Particle Image Velocimetry (PIV). Although two separate runs have to be performed to gather both kinds of data, a rather comprehensive representation of the flow is obtained in this way. In particular, the bubble size is needed as an input to the computational model. To capture changes in the flow with the bubble size as well as gas- and liquid flow rates, variations of these three quantities are considered. Of the large number of different test conditions examined experimentally, six cases have been selected for the present work to highlight some qualitative features of the flow, leaving a broader parametric study for the future.

The CFD simulations are largely based on physical models used previously with success for a variety of bubble columns and bubbly pipe flows (e.g. Rzehak et al. 2017 and references therein). Different correlations for the drag and lift force acting on the bubbles are evaluated for the present application. While good agreement between experiment and simulation can be obtained for the gas-fraction and -velocity by choosing a drag force correlation appropriate for the water quality, the calculated liquid-velocity is found too large in particular at the smaller bubble sizes.

2 BUBBLE COLUMN SET-UP

2.1 Geometry

The shadow imaging and PIV measurements have been executed in a quadratic laboratory-scale bubble column made of acrylic glass with an inner side length of D = 0.100 m and a height of H = 2 m (Figure 1a). It comprises 6 main parts: two 0.535 m long inlet and outlet sections (Figure 1a, #1 and #2), the water inlet through four 1" pipes on top (Figure 1a, #3), a 2 m high acrylic pipe for gas ventilation on top of the column with an inner diameter of 0.04 m (Figure 1a, #4), the 1 m long effective measurement section (Figure 1a, #5 and Figure 1b) and an interchangeable gas distributor (Figure 1a, #6 and Figure 1c). The distributor consists of 7 capillaries placed in line with 12.5 mm equal spacing in the center of the bubble column. Bubbles in a size range of 1 to 9 mm are produced by introducing air through capillaries of different diameter and material (0.13 mm / stainless steel, 0.18 mm / Teflon and 3.6 mm / PEEK). The nozzles are separately connected to seven magnetic valves (Type 6712, Bürkert), which are supplied by a mass flow controller (F-201CV, Bronkhorst) and the pressurized gas pipeline.

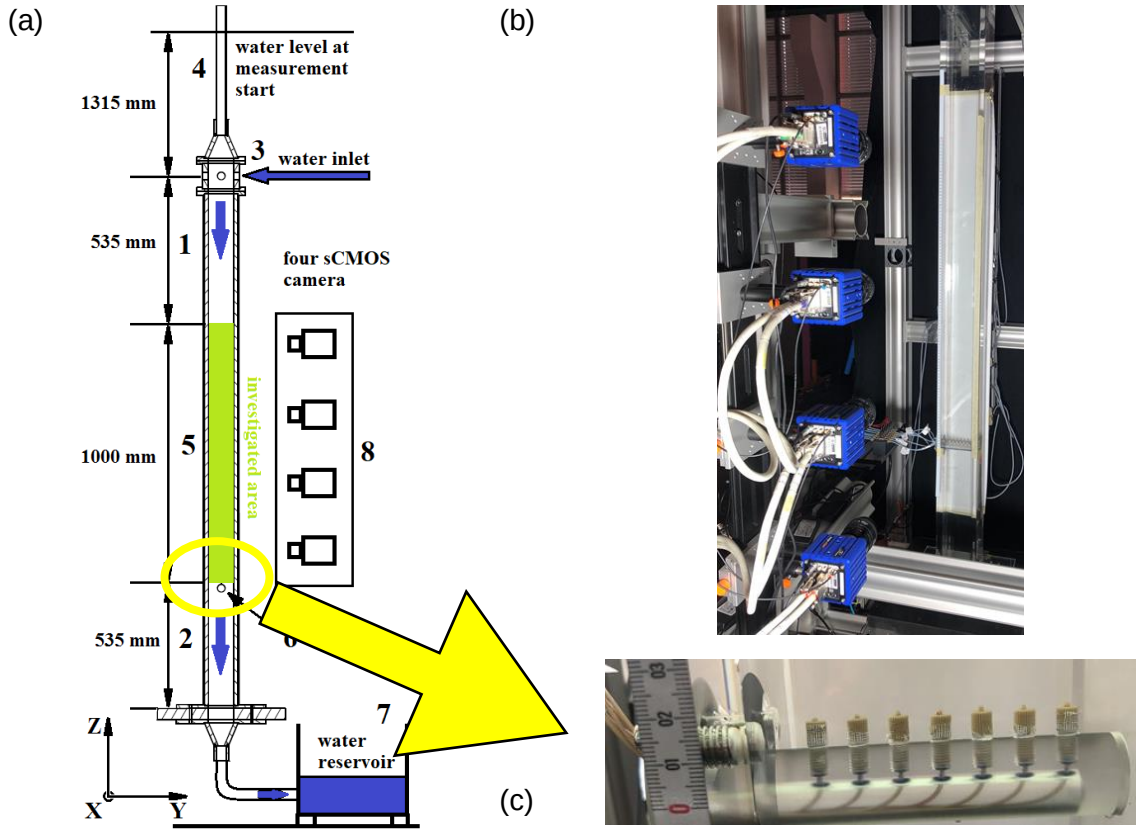

Figure 1: Experimental set-up: (a) schema, (b) photograph, (c) gas distributor.

In order to avoid pulsations induced by a pump, the countercurrent water flow is driven by gravity from an upper water reservoir situated about 4 m above the bottom water reservoir. This set-up allows a maximum water flow rate of Q_L = 55.5 l min^{-1}, which corresponds to a Reynolds number of Re = 9000 inside the bubble column. The column Reynolds number is defined as $Re = (\rho_L J_L D_H)/\mu_L$, where ρ_L is the liquid density, J_L is the superficial liquid velocity,

D_H is the hydraulic diameter of the column and μ_L is the dynamic viscosity of the liquid. All measurements were done at atmospheric pressure and room temperature.

2.2 Materials and flow parameters

The water was de-ionized with an ion-exchange resin column, filled into the water reservoir and pumped through the whole system. After this procedure, the conductivity of the water was measured and always remained below 30 µS/cm.

Five different countercurrent liquid flow rates were investigated, of which the smallest and largest are selected for the present investigation to show the effect of the counter-current flow. Three different values of gas flow rate were set which depended on the nozzle size through which the gas was supplied. Only the medium flow rate is selected presently to limit the computational effort required for the simulations. Depending on the size and material of the nozzles through which the gas was supplied, bubbles of different size were produced. All different capillary types are included in the present study to represent the effect of bubble size on the flow. A summary of parameters for all six cases considered in this comparison is given in Table 1.

Table 1: Investigated flow conditions.

Case Name	Nozzle diameter / material [mm]	Gas volume flow rate Q_G [l h^{-1}]	Gas superficial velocity J_G [m s^{-1}]	Liquid volume flow rate Q_L [l min^{-1}]	Liquid superficial velocity J_L [m s^{-1}]	Column Reynolds number Re [-]	Mean bubble diameter d_B [mm]
S21	0.13 mm / stainless steel	6	$1.7 \cdot 10^{-4}$	0.6	$1 \cdot 10^{-3}$	100	2.1
S25	0.13 mm / stainless steel	6	$1.7 \cdot 10^{-4}$	55.5	$9.3 \cdot 10^{-2}$	9000	2.2
M21	0.18 mm / Teflon	6	$1.7 \cdot 10^{-4}$	0.6	$1 \cdot 10^{-3}$	100	3.3
M25	0.18 mm / Teflon	6	$1.7 \cdot 10^{-4}$	55.5	$9.3 \cdot 10^{-2}$	9000	3.6
L21	3.6 mm / PEEK	29	$8.1 \cdot 10^{-4}$	0.6	$1 \cdot 10^{-3}$	100	6.4
L25	3.6 mm / PEEK	29	$8.1 \cdot 10^{-4}$	55.5	$9.3 \cdot 10^{-2}$	9000	6.4

2.3 Measurement systems

To characterize the gas and liquid flow in the bubble column, two different optical measurement methods have been applied. First, the characteristics of the bubbles, such as bubble diameter, velocity, shape or position were measured with shadow imaging. This technique is based on particle shadow recognition combined with Particle Tracking Velocimetry (PTV) to measure the velocity of the bubbles. Then, for the liquid phase, PIV was used to examine the velocity fields of the continuous phase.

2.3.1 Bubble parameters

For the shadow imaging measurements, four Imager sCMOS cameras (LaVision, Figure 1a, #8 and Figure 1b) were used with a 2560 x 2160 pixels resolution and 80 Hz frame rate. They were arranged in a vertical line one above each other, to simultaneously record all bubbles over the entire measurement section (1 m). The cameras were focused to the center of the column and, due to the depth of field (DOF), bubbles were identified in a 33 mm thick middle region. Eight high-power, pulsed COB LEDs (Luminus CXM-32) with an overall nominal power of 1140 W were used together with a sheet of thin drawing paper, as light diffuser on the back wall of the column, to obtain homogeneous light distribution. The geometrical calibration was performed in the whole measurement area with a 3D calibration plate. With this experimental setup, 4x1000 pictures were taken for each investigated case.

The recorded images were processed in DaVis 8.4 (LaVision) with a built-in shadow image processing tool, combined with a PTV algorithm. The detailed image processing steps can be found in (Kováts et al., 2020). Employing the distinct intensity gradients at the border of the focused and unfocused bubbles, only those bubbles were recognized, which were situated in the focused volume (33 mm) in the middle of the column. From the processed data, the bubble positions as well as mean equivalent sphere diameters and velocities and their distributions have been obtained by further post-processing with Matlab. The distribution of mean equivalent sphere diameters is rather narrow. Its mean values throughout the column for the considered cases are listed in Table 1. From the bubble positions and volumes, the gas fraction has been calculated on a grid by the same method as in Rzehak et al. (2017a).

2.3.2 Liquid velocity

For the PIV measurements, the same camera set-up was used as before, but the cameras were equipped with band-pass filters (590 nm, 50 nm FWHM) to record only the fluorescence signal of the Rhodamin B doped polymethyl methacrylate (PMMA) seeding particles (diameter: 1-20 µm). These particles were excited by a double-pulse Nd:YAG laser (Quantel Evergreen) at 532 nm with 40 mJ/pulse. The laser beam was divided into two beams with a 50-50% mirror and these two beams were then expanded by two light sheet optics placed above each other, to illuminate equally the whole 1 m measurement section. The geometrical positions were calibrated with a 3D calibration target over the whole measurement section. Overall, 4000 experimental images were acquired with 5 Hz in double frame mode for each investigated condition. The delay time between the two frames was 11 ms.

From the recorded double-frame images, flow fields were calculated in DaVis. For the vector calculation, a cross-correlation (multi-pass, decreasing size) PIV algorithm was used with an interrogation window size from 64x64 pixels to 32x32 pixels, with 50% overlap. To remove false vectors and refine the vector field, especially in the vicinity and shadows of the bubbles, a median filter was applied. The instantaneous vector fields, processed like this, were averaged in time and the resulting mean flow fields were used for the comparison with the numerical results.

3 DESCRIPTION OF SIMULATIONS

The Euler-Euler two-fluid framework is based on a set of conservation, i.e. continuity and Navier-Stokes, equations for each phase, gas (index 'G') and liquid (index 'L'). A number of monographs detailing the derivation of these equations are available (e.g. Drew and Passman 1998, Yeoh and Tu 2010, Ishii and Hibiki 2011). For the sake of completeness these are summarized as follows:

$$\frac{\partial}{\partial t}(\alpha_G \rho_G) + \nabla \cdot (\alpha_G \rho_G \boldsymbol{u}_G) = 0, \tag{1}$$

$$\frac{\partial}{\partial t}(\alpha_L \rho_L) + \nabla \cdot (\alpha_L \rho_L \boldsymbol{u}_L) = 0, \tag{2}$$

$$\frac{\partial}{\partial t}(\alpha_G \rho_G \boldsymbol{u}_G) + \nabla \cdot (\alpha_G \rho_G \boldsymbol{u}_G \otimes \boldsymbol{u}_G) = -\alpha_G \nabla p_G + \nabla \cdot (\alpha_G \mathbf{T}_G) + \alpha_G \rho_G \boldsymbol{g} + \boldsymbol{F}_G^{inter}, \tag{3}$$

$$\frac{\partial}{\partial t}(\alpha_L \rho_L \boldsymbol{u}_L) + \nabla \cdot (\alpha_L \rho_L \boldsymbol{u}_L \otimes \boldsymbol{u}_L) = -\alpha_L \nabla p_L + \nabla \cdot (\alpha_L \mathbf{T}_L) + \alpha_L \rho_L \boldsymbol{g} + \boldsymbol{F}_L^{inter}. \tag{4}$$

In Eqs. (3) and (4) terms requiring closure are the interfacial forces $\boldsymbol{F}^{inter}$ and the stress tensors $\mathbf{T}$. For the interfacial forces the relation $\boldsymbol{F}_G^{inter} = -\boldsymbol{F}_L^{inter}$ holds due to overall momentum conservation. Therefore, only one of them needs to be prescribed. The stress tensor is taken as that for a Newtonian fluid

$$\mathbf{T} = \mu^{eff}\left(\nabla \boldsymbol{u} + (\nabla \boldsymbol{u})^T - \frac{2}{3}(\nabla \cdot \boldsymbol{u})\mathbf{I}\right), \tag{5}$$

with turbulence taken into account by the effective dynamic viscosity $\mu^{eff} = \mu^{mol} + \mu^{turb}$. The closure relations largely follow a baseline model that was successfully used in a number of previous investigations on bubbly flows comprising bubble and airlift columns (Ziegenhein et al. 2013, 2017, Liao et al. 2016, Rzehak et al. 2017a, Fleck and Rzehak 2019), pipe flows (Rzehak et al. 2015, Rzehak and Krepper 2015, Rzehak and Kriebitzsch 2015), static mixers (Zidouni et al. 2015) and stirred tanks (Shi and Rzehak, 2018). Accordingly, the interfacial force comprises a number of contributions summarized in Table 2 together with the closure correlation used for each. The turbulent dynamic viscosity μ^{turb} for the liquid phase is calculated from a k-ω SST model (Menter 2009) with additional source terms accounting for the bubble-induced turbulence (Ma et al. 2017), while for the gas phase turbulence is neglected by setting $\mu^{turb} = 0$. A detailed description of the model is available in Rzehak et al. (2017).

Table 2: Summary of bubble force correlations for the baseline model.

force	reference
drag	Ishii and Zuber (1979)
shear lift	Hessenkemper et al. (2021)
wall lift	Hosokawa et al. (2002)
turbulent dispersion	Burns et al. (2004)
virtual mass	constant coefficient C_{VM} = ½

One change that has been made in the baseline model compared to the quoted previous works was to update the lift force model from the older one due to Tomiyama et al. (2002) to

the one recently proposed by Hessenkemper et al. (2021). For the sake of definiteness, expressions for the lift coefficient in terms of dimensionless numbers $Re_B = \rho_L \, u_{rel} \, d_B/\mu_L$ and $Eo_B = (\rho_L - \rho_G) g d_B^2/\sigma$ are spelled out as follows.

For the model from Tomiyama et al. (2002), which was based on experiments with air bubbles in a glycerol water solution, the lift coefficient is given by

$$C_L = \begin{cases} \min[0.288 \tanh(0.121\, Re_B), f(Eo_\perp)] & Eo_\perp < 4 \\ f(Eo_\perp) & \text{for} \quad 4 < Eo_\perp < 10 \\ -0.27 & 10 < Eo_\perp \end{cases} \tag{6}$$

$$\text{with } (Eo_\perp) = 0.00105\, Eo_\perp^3 - 0.0159\, Eo_\perp^2 - 0.0204\, Eo_\perp + 0.474\,.$$

Here the modified Eötvös number is defined by $Eo_\perp/Eo_B = (d_\perp/d_B)^2$, where the horizontal bubble dimension is determined from the empirical correlation for the aspect ratio given by Wellek et al. (1966), i.e.

$$d_\perp = d_B \sqrt[3]{1 + a\, Eo_B^b} \tag{7}$$

with constants $a = 0.163$ and $b = 0.757$.

For the model of Hessenkemper et al. (2021), two expressions were combined. One that depends on the modified Eötvös number $Eo_\perp$but with different constants $a = 0.65$ and $b = 0.35$, which was based on original experiments with air bubbles in water, and one depending on the bubble Reynolds number Re_B and the non-dimensional shear rate $Sr = d_B|\omega|/u_{rel}$ proposed by Legendre and Magnaudet (1998) based on DNS simulations. The combined lift coefficient is

$$\begin{aligned} &C_{L,G} = f(Sr, Re_B) - f(Eo_\perp) \\ &\text{with } f(Sr, Re_B) + \left(\left(\frac{6}{\pi^2} \frac{1}{\sqrt{Re_B\, Sr}} \frac{2.255}{(1 + 0.2 Sr/Re_B)^{3/2}} \right)^2 + \left(\frac{1}{2} \frac{Re_B + 16}{Re_B + 29} \right)^2 \right)^{1/2} \\ &\text{and } f(Eo_\perp) = \frac{\ln\left(1 + \exp\left(-12(g)\right)\right)}{12}, \\ &\qquad g = 0.11 \frac{\ln(1 + \exp(4(Eo_\perp - 5.6)))}{4} - 0.14(Eo_\perp - 5.2) - 0.44. \end{aligned} \tag{8}$$

One reason to prefer the latter of the two models are that it is based on experiments using water as the liquid, which gives a Morton number $Mo \approx 10^{-11}$, while the former was based on experiments in glycerol water solutions with much higher values of $Mo \approx 10^{-2.8} \ldots 10^{-5.5}$. Furthermore, for small bubbles of spherical shape the correlation from Tomiyama et al. (2002) violates other established results (e.ge Shi et al. 2020 and references therein), which show an increase rather than a decrease of the lift coefficient as the bubble size is reduced.

A graphical comparison for the lift coefficient C_L as a function of the bubble size d_B for air bubbles in water according to both models is shown in Figure 2. It is seen that both models share the important feature that the lift coefficient becomes negative at a certain bubble size, which has a significant impact on the distribution of gas fraction (Lucas and Tomiyama 2011), while quantitative differences between the models are moderate.

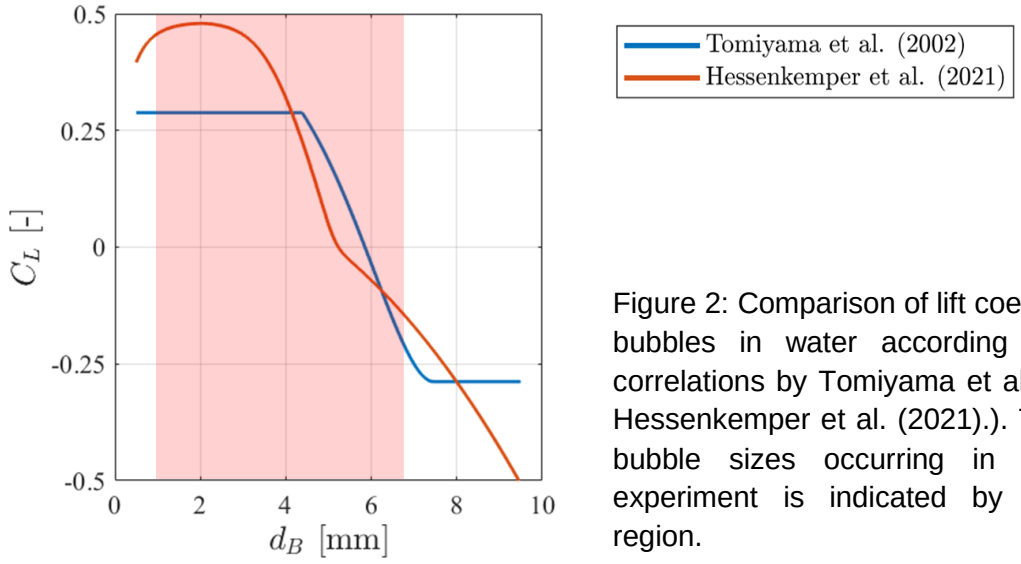

Figure 2: Comparison of lift coefficient for air bubbles in water according to the two correlations by Tomiyama et al. (2002) and Hessenkemper et al. (2021).). The range of bubble sizes occurring in the present experiment is indicated by the shaded region.

In the course of the investigation it was found that the baseline model of Table 2 underpredicted the relative velocity between gas and liquid phases for a number of cases. This could be attributed to the water quality, which is well-known to affect the terminal velocity of gas bubbles. A set of correlations for the drag coefficient C_D that applies to different qualities of water was proposed by Tomiyama et al. (1998) and will be evaluated as an alternative to the correlation from Ishii and Zuber (1979) applied in previous works (see Table 2).

The correlation proposed by Ishii and Zuber (1979) distinguishes three regimes for spherical, ellipsoidal and cap-shaped bubbles according to

$$C_D = max\{C_{D,sphere}, min[C_{D,ellipse}, C_{D,cap}]\}\,, \tag{9}$$

where,

$$C_{D,sphere} = \frac{24}{Re_B}(1 + 0.1\,Re^{0.75})$$

$$C_{D,ellipse} = \frac{2}{3}\sqrt{Eo}$$

$$C_{D,cap} = \frac{8}{3}.$$

In the correlations from Tomiyama et al. (1998) the ellipsoidal and cap-shaped regimes are combined into a single one with a smooth variation of the drag coefficient, while modifications are introduced for the spherical regime to account for three different qualities of the water.

For contaminated water:

$$C_D = max\left\{\frac{24}{Re_B}(1 + 0.15\,Re_B^{0.687}),\ \frac{8}{3}\ \frac{Eo}{Eo + 4}\right\} \tag{10}$$

For slightly contaminated water:

$$C_D = max\left\{min\left[\frac{24}{Re_B}(1 + 0.15\,Re_B^{0.687}),\ \frac{72}{Re_B}\right],\ \frac{8}{3}\ \frac{Eo}{Eo + 4}\right\} \tag{11}$$

For pure water:

$$C_D = max\left\{min\left[\frac{16}{Re_B}(1 + 0.15\, Re_B^{0.687}),\ \frac{48}{Re_B}\right],\ \frac{8}{3}\ \frac{Eo}{Eo + 4}\right\} \tag{12}$$

For a quantitative comparison, the terminal velocity of air bubbles in water as calculated from all four correlations is shown in Figure 3. It is seen that for bubbles smaller than 2.3 mm there is only a negligible difference between the correlation from Ishii and Zuber and the contaminated case from Tomiyama et al., while for larger bubbles, the difference is small but noticeable. On the other hand, a difference between the pure and slightly contaminated cases from Tomiyama et al. exists only for bubbles smaller than 1.3 mm.

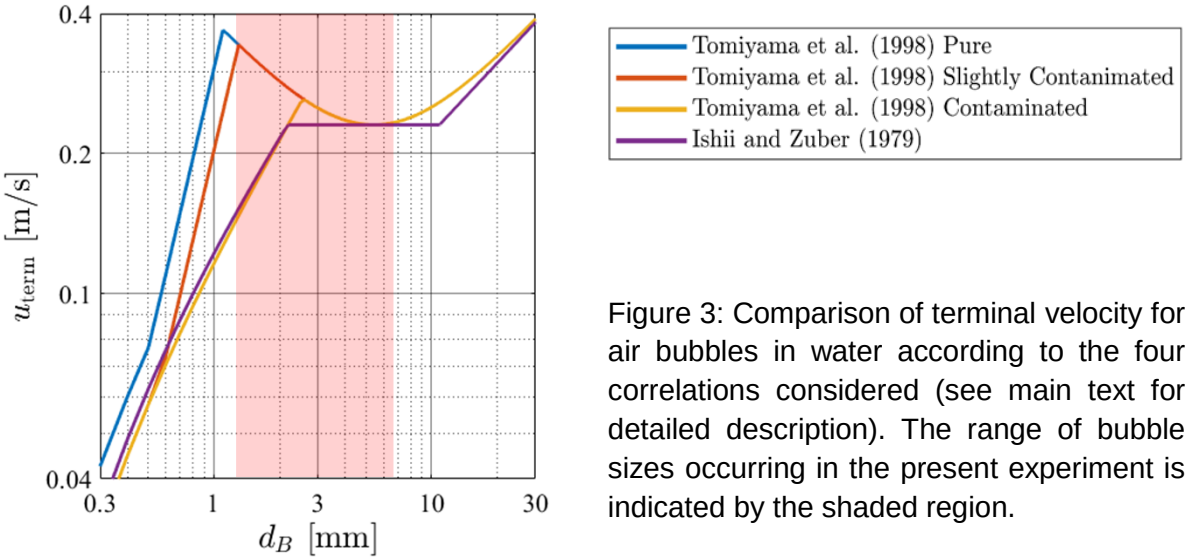

Figure 3: Comparison of terminal velocity for air bubbles in water according to the four correlations considered (see main text for detailed description). The range of bubble sizes occurring in the present experiment is indicated by the shaded region.

Further relations, needed to complete the system of equations are the expression for overall volume conservation, $\alpha_G + \alpha_L = 1$, and the assumption of pressure equilibrium, $p_G = p_L$.

Both phases, gas and liquid are assumed to be incompressible fluids with constant properties. Their values corresponding to air and water at ambient conditions are given in Table 3. The gas phase is treated as monodisperse with bubble sizes taken from the experiment for each case (see Table 1).

Table 3: Summary of material properties.

ρ_L	997	kg / m³
μ_L	8.899e-4	kg / (m s)
ρ_G	1,185	kg / m³
μ_G	1.831e-5	kg / (m s)
σ	0.072	N / m

The simulations are performed on a fully three-dimensional domain comprising the region where measurements were taken, i.e. a section of 1m height above the nozzles supplying the gas, extended by the 0.535 m inlet and outlet sections (see Figure 1). These extensions provide flow

development or abatement zones to eliminate the influence of the boundary conditions imposed at top and bottom of the domain. The nozzles supplying the gas are treated as point sources.

Boundary conditions for counter-current flow (see e.g. Khan et al. 2023) impose a uniform liquid velocity directed out of the domain at the bottom and constant pressure together with vanishing tangential velocity components and a vanishing normal derivative of gas fraction at the top plane. On the solid side walls of the column, a no-slip condition is set for the liquid velocity, while a free slip condition is prescribed for the gas velocity assuming that direct contacts between the bubbles and the walls are negligible. The need to resolve the viscous boundary layer is circumvented by using a single phase turbulent wall function for a smooth wall.

The simulations are performed using OpenFoam v10 (OpenFoam 2022) together with the HZDR add-on (Schlegel et al. 2023). A uniform mesh with 40 x 40 x 300 points corresponding to a spacing of 2.5 x 2.5 x 6.7 mm along the x- , y-, and z-axes is used. The simulations are run for a total time of 500 s for the small and medium nozzle cases and 800 s for the large nozzle cases with an adjustable timestep keeping a Courant number of 0.5. The results are then averaged from 250 s until the end of the simulation time.

4 RESULTS AND DISCUSSION

In this section, experimental and simulation results are compared. Data are taken in a plane spanned by the horizontal x-direction along the nozzles and the vertical z-direction (see Figure 1), which extends from the nozzles to a height of 1.0 m. The y-direction along the depth of the column is not resolved in the measurements. The origin of coordinates is chosen such that the lower left corner of the measurement plane appears at $x = 0, y = D/2, z = 0$. Coordinates scaled by the width D of the column are used throughout the following representations. For the gas fraction α_G and the vertical component of the gas velocity w_G, the simulation results are averaged in the y-direction over a region corresponding to the depth of field (DOF) of the camera used in the shadow measurements. For the vertical component of the liquid velocity w_L no such averaging is necessary since the laser light sheet used for PIV in the liquid is thin. The vertical component of the relative velocity $w_{rel} = w_G - w_L$ is also shown in the following.

The first subsection 4.1 is concerned with a comparison of the different drag model described in Section 3. Since their influence is most significant at small bubble size, cases from the nozzle set with the smallest diameter are used. Subsection 4.2 considers the development of the flow along the height of the column as well as the three-dimensional flow structure including the depth of the column. Since no measurements were taken along that direction, the simulated results are used to provide at least a qualitative picture. The medium-sized nozzle cases are used for this purpose. Section 4.3 finally covers the cases with the largest nozzle diameter to complete this first overview of the entire database. Interest in these cases comes from the fact that the bubble size is large enough to cause the lift force according to Tomiyama et al. (2002) to change its direction, pointing away from the column walls rather than towards them.

4.1 Comparison of drag laws

Water quality is well-known to have a significant impact on the bubble rise velocity. As discussed in Section 3, the baseline model of Eq. (9) proposed by Ishii and Zuber (1979) and used in many previous simulation studies applies to contaminated water. A set of models given in Eqs. (10) - (12) comprising different water qualities was proposed by Tomiyama et al. (1998). Results of simulations based on all of these four models are shown in Figure 4 and Figure 5 for cases S21and S25 with mean bubble sizes of d_B = 2.1 and 2.2 mm, respectively, in the center of the measurement section at z = 0.5 m.

Comparing the simulation results for all models confirms that for this bubble size range the baseline model from Ishii and Zuber (1979) and the model for contaminated water from Tomiyama et al. (1998) give identical results shown in Figure 4 for case S25 with the higher liquid flow rate. In Figure 3 for case S21 with the lower liquid flow rate, small deviations are seen in all quantities except for the relative velocity, represented together with the gas velocity in the lower left figure. The differences are most prominent in the liquid velocity and presumably of a statistical nature, i.e. they would decrease for a longer averaging period. In a similar way, it is confirmed that for these bubble sizes, models for pure and slightly contaminated water from Tomiyama et al. (1998) agree with each other.

Comparison with the experimental data shows that for both cases the latter correlations for pure and slightly contaminated water provide good agreement for the gas fraction and gas velocity, while the other two show appreciable deviations. In particular, the gas fraction is overpredicted and the gas and relative velocities are underpredicted. Since the gas fraction is

inversely proportional to the residence time of the bubbles in the column and the latter is proportional to the gas velocity, these corresponding observations must be expected. In contrast, the liquid velocity is overpredicted by all models, up to a factor of three for the lower liquid flowrate (case S21) and by ~15% for the higher liquid flowrate (case S25). However, in both cases the liquid flow rate is an order of magnitude smaller than the relative velocity, which means that its deviation has only little influence on the gas phase properties. The simulated relative velocity for all models is constant over the entire column width and its value agrees closely with the respective terminal velocity from Figure 3. The measured relative velocity is also rather constant over the column width, except very close to the walls and only slightly larger than the simulated one.

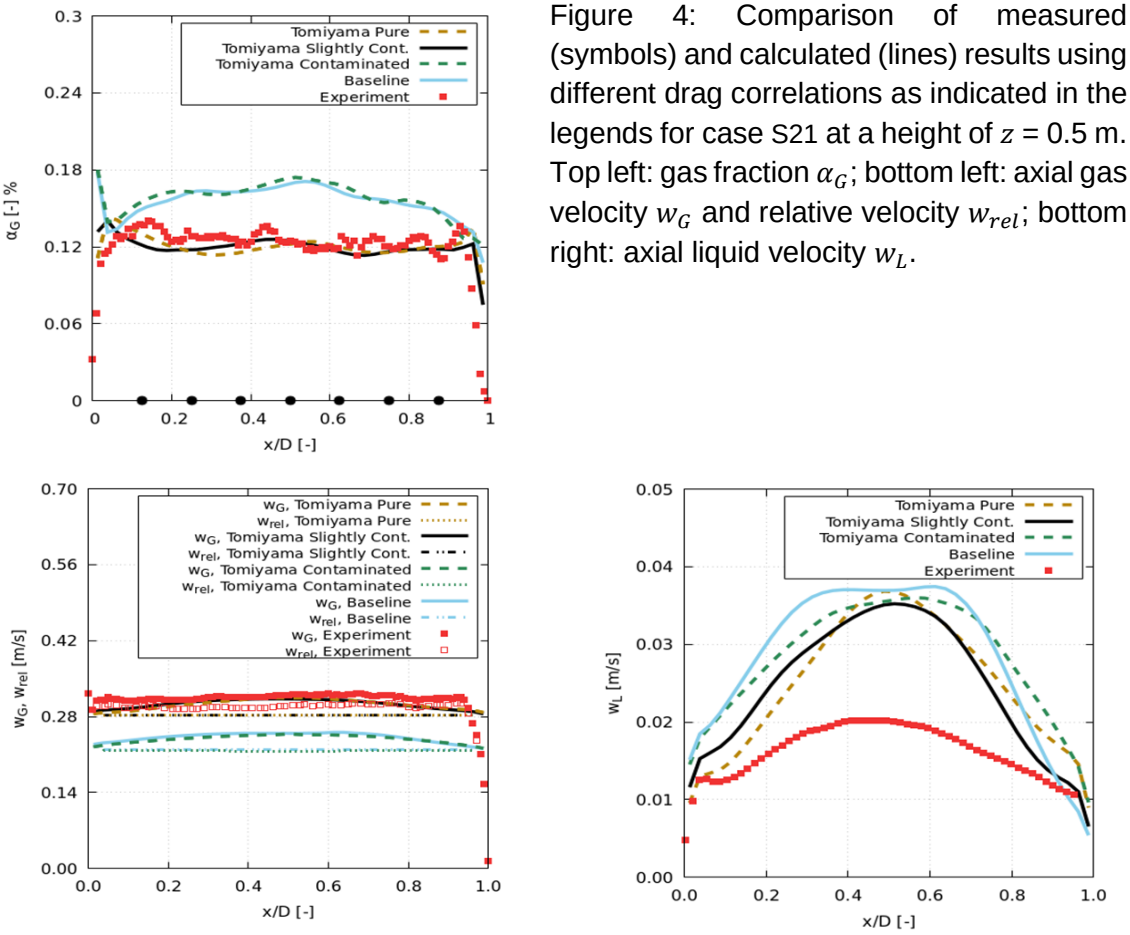

Figure 4: Comparison of measured (symbols) and calculated (lines) results using different drag correlations as indicated in the legends for case S21 at a height of z = 0.5 m. Top left: gas fraction α_G; bottom left: axial gas velocity w_G and relative velocity w_{rel}; bottom right: axial liquid velocity w_L.

Concerning bubbles of larger size than for the two cases considered up to now, it may be added, that based on Figure 3, the difference between fully and slightly contaminated models from Tomiyama et al. (1998) disappears for larger bubbles with $d_B \gtrsim 2.5$ mm and only a small difference remains between these models and the baseline model with the correlation from Ishii and Zuber (1979). In summary it may be said that the correlation for slightly contaminated bubbles from Tomiyama et al. (1998) applies well for the present conditions and is in accord with the way the water was prepared for the experiment (see section 2.2). Hence this model will be used for the rest of the investigation.

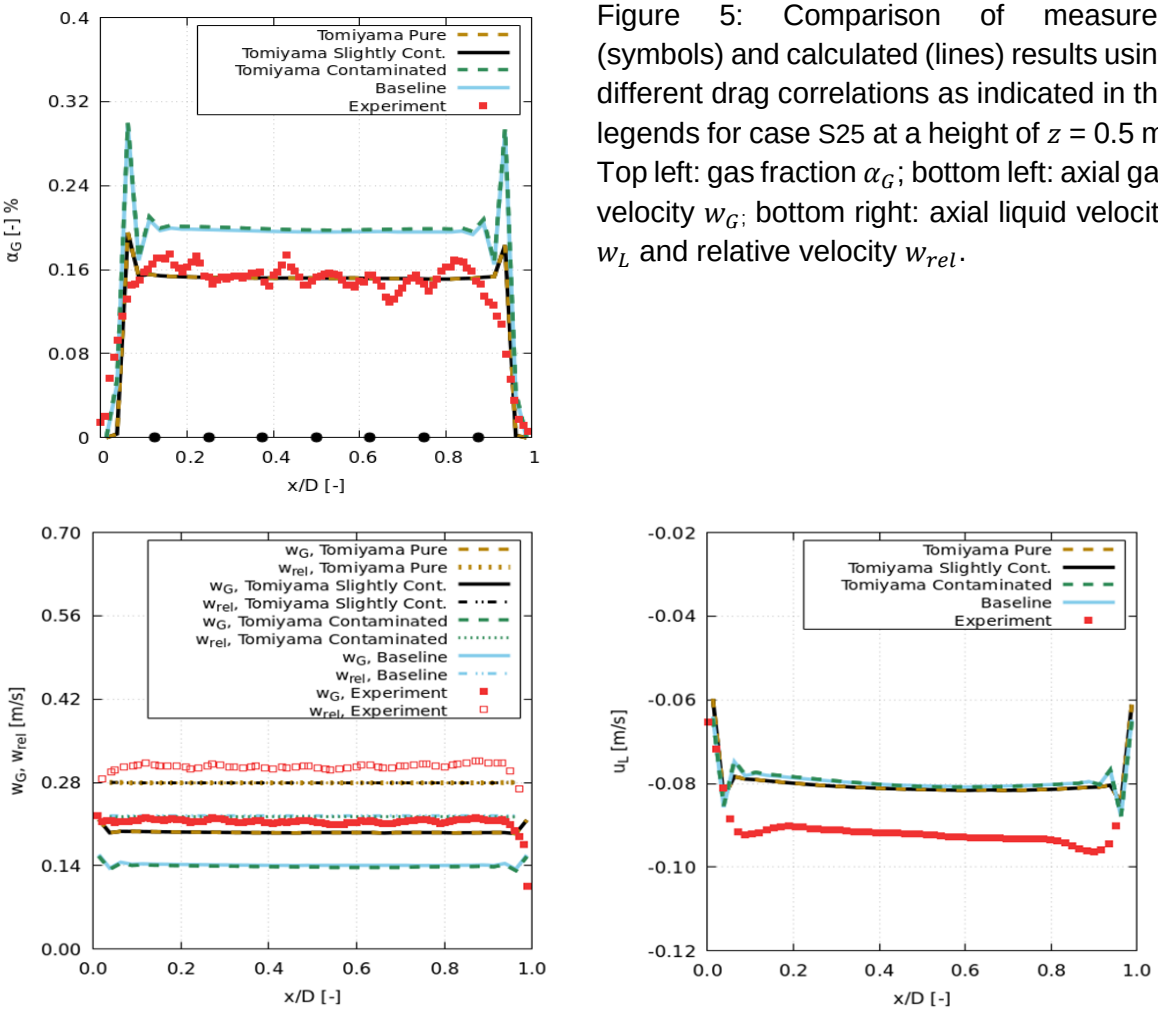

Figure 5: Comparison of measured (symbols) and calculated (lines) results using different drag correlations as indicated in the legends for case S25 at a height of z = 0.5 m. Top left: gas fraction α_G; bottom left: axial gas velocity w_G; bottom right: axial liquid velocity w_L and relative velocity w_{rel}.

4.2 Investigation of flow structure

The development of the flow over the height of the column is investigated in this section for cases M21 and M25 with mean bubble sizes of d_B = 3.3 and 3.6 mm. As already mentioned, only the slightly contaminated drag law from Tomiyama et al. (1998) is considered, which was found adequate for smaller bubble sizes in the previous section. On the other hand, only minor differences between the drag models appear for bubbles in the size range considered here. As described in Section 3 the newer lift force model from Hessenkemper et al. (2021), Eq. (8), has been adopted as the baseline model for the present investigation. However, to make connection with earlier simulations using the model of Tomiyama et al. (2002), Eq. (6), a comparison of both models is included at the end of this section.

Profiles of gas fraction α_G at four different heights z = 0.1, 0.2, 0.5, 1.0 m above the nozzles are shown in Figure 6. In both cases considered here, a slight decrease of α_G with height is observed, which is well captured by the simulations. At the lowest height, a clear signature of the individual nozzles is visible in both, simulation and experiment. In the experiment, this signature has different magnitudes for the different nozzles, which indicates slight differences in the bubble stream produced by each nozzle. Of course such differences are absent in the simulations. In the experiment, remainders of this signature are present as a statistical variation throughout the measurement plane, while in the simulations they are smoothed out already shortly above the nozzles. At the highest level, a small wall peak is visible in the

experimental data, which is located about halfway between the column wall and the nearest nozzle. This wall peak is clearly seen in the simulations as well. However, the simulations show a distinguished peak also at the lower heights, where its presence in the measured data is less clear due to the remaining nozzle signature. Both the steep rise of the measured gas fraction from the column wall towards the mentioned wall peaks and the roughly constant region between them (aside from the remnants of the nozzle signature) are well reproduced by the simulations.

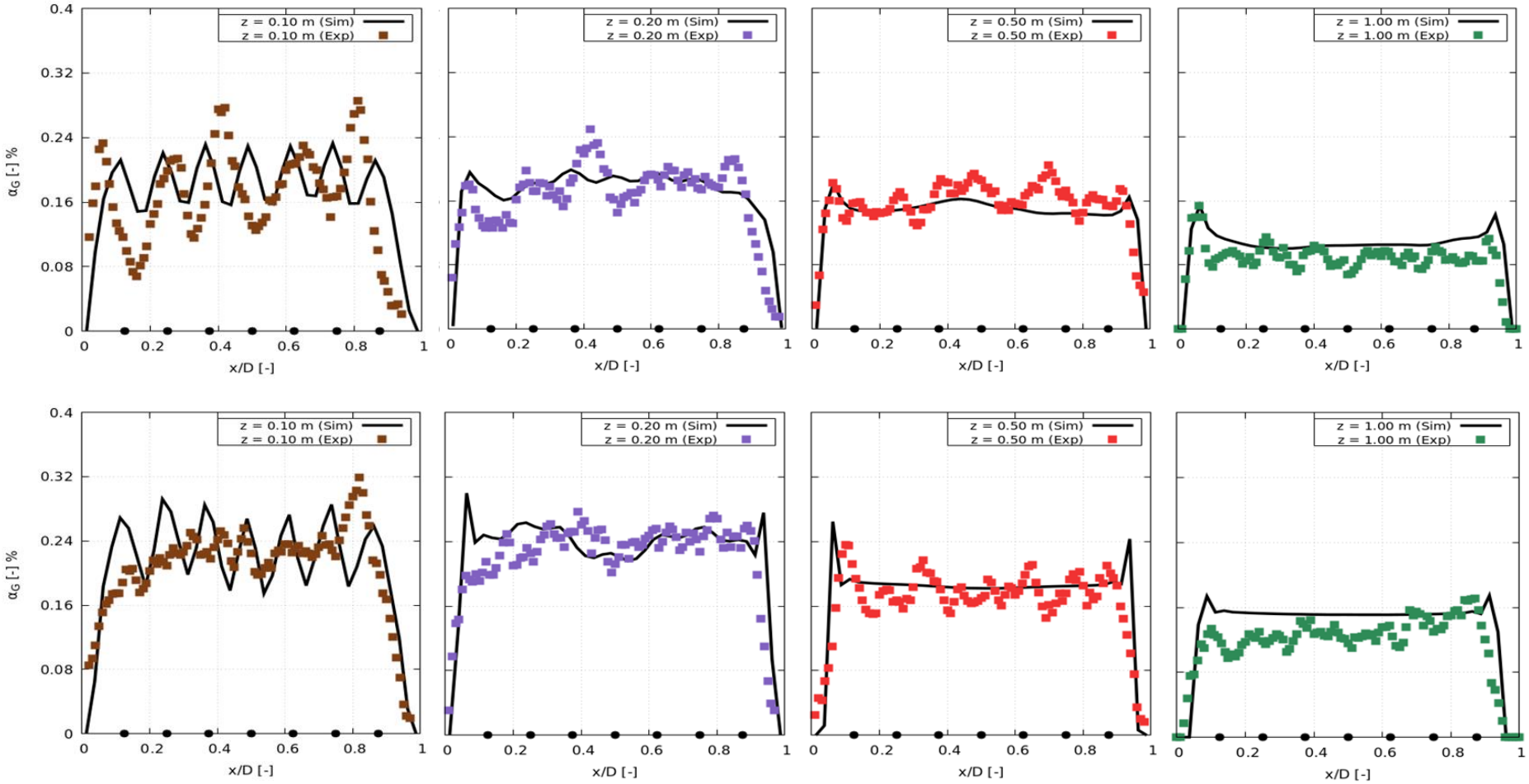

Figure 6: Profiles of gas fraction α_G at heights z = 0.1, 0.2, 0.5, 1.0 m (from left to right) above the nozzles supplying the gas as indicted by the black points on the x-axis. Top row: case M21; bottom row: case M25. Symbols: measured data; lines: simulation results.

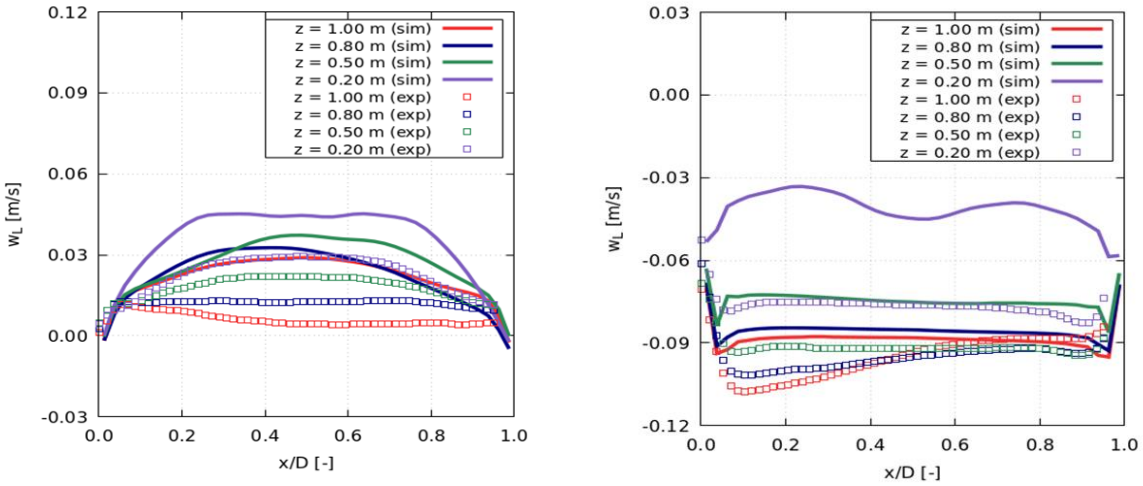

Figure 7: Comparison between measured (symbols) and calculated (lines) radial profiles of liquid velocity, w_L, for case M21 (left) with low liquid flow rate, Re = 100, and case M25 (right) with high liquid flow rate, Re = 9000. Mind the different scales for both cases.

Figure 7 shows profiles of liquid velocity w_L at four heights z = 0.2, 0.5, 0.8 and 1.0 m. In the experimental data, an asymmetric shape is seen at the highest level for case M21 and the two highest levels for case M25, despite the mirror symmetry of the column geometry. This most likely stems from the liquid inlet, which is supplied through four pipes, one in each sidewall, at the top of the column ~0.5 m above the measurement region. Apparently this inlet causes a dynamic symmetry breaking, which may persist down to a height of z = 0.5 m depending on the experimental parameters. This symmetry breaking is of course not captured by the present simulations, which impose a homogeneous liquid flow. At the lower levels $z \leq 0.5$ m the shape of the profiles is reproduced well by the simulation. However, a quantitative comparison shows that the simulated liquid velocities are systematically too high, by a factor of 2 for the lower liquid flow rate (case M21) and by ~15% for the higher liquid flow rate (case M25), which corresponds to the factors also found for the smaller bubble size cases from section 4.1.

Further light on the origin of the deviation between calculated and measured liquid velocities is shed by analyzing the two-dimensional plots of the liquid velocity up to a height of z = 0.5 m in Figure 8. The plots of the x-z plane (left) show the flow fields in the measurement plane, while the plots of the y-z plane (right) reveal the flow structure perpendicular to the measurement plane, where unfortunately no experimental data are available. Two different flow regimes are clearly distinguishable in these plots. For case M21 (left), the liquid counterflow is weak enough to be overcome by the bubbles dragging the liquid upwards in a region around the column center over the entire investigated height. Downward flow of liquid in this regime occurs only in the front and back regions of the column. Therefore, for this case the liquid velocity profile at y = 0 shown in the left part of Figure 7 is directed entirely upwards. For case M25 in contrast, an upwards directed liquid flow is only seen within a short distance from the nozzles, while at higher elevations, the liquid flow is directed downwards throughout the depth of the column. This explains why only negative velocities appear in the right part of Figure 7, where only heights starting from z = 0.2 m are considered. A downward flow occurs not only in the back and front of the column but also on the left and right. It should be noted that in all cases, the bubbles continue to rise upwards since the magnitude of the liquid flow velocity always remains smaller than the bubble terminal velocity.

Clearly in both regimes, the effect on the liquid velocity strongly depends on the spread of the bubbles along the depth of the column. If these are more concentrated in the column center, the reversed (upwards) liquid flow will be stronger but also more confined. Thus an inaccuracy of the models to correctly predict the spreading of the bubbles will result in a corresponding inaccuracy of the liquid velocity in the column center along the depth (y-direction). The previously noted overprediction of liquid velocities in Figure 7 is thus likely related to a too narrow gas fraction profile along the column depth.

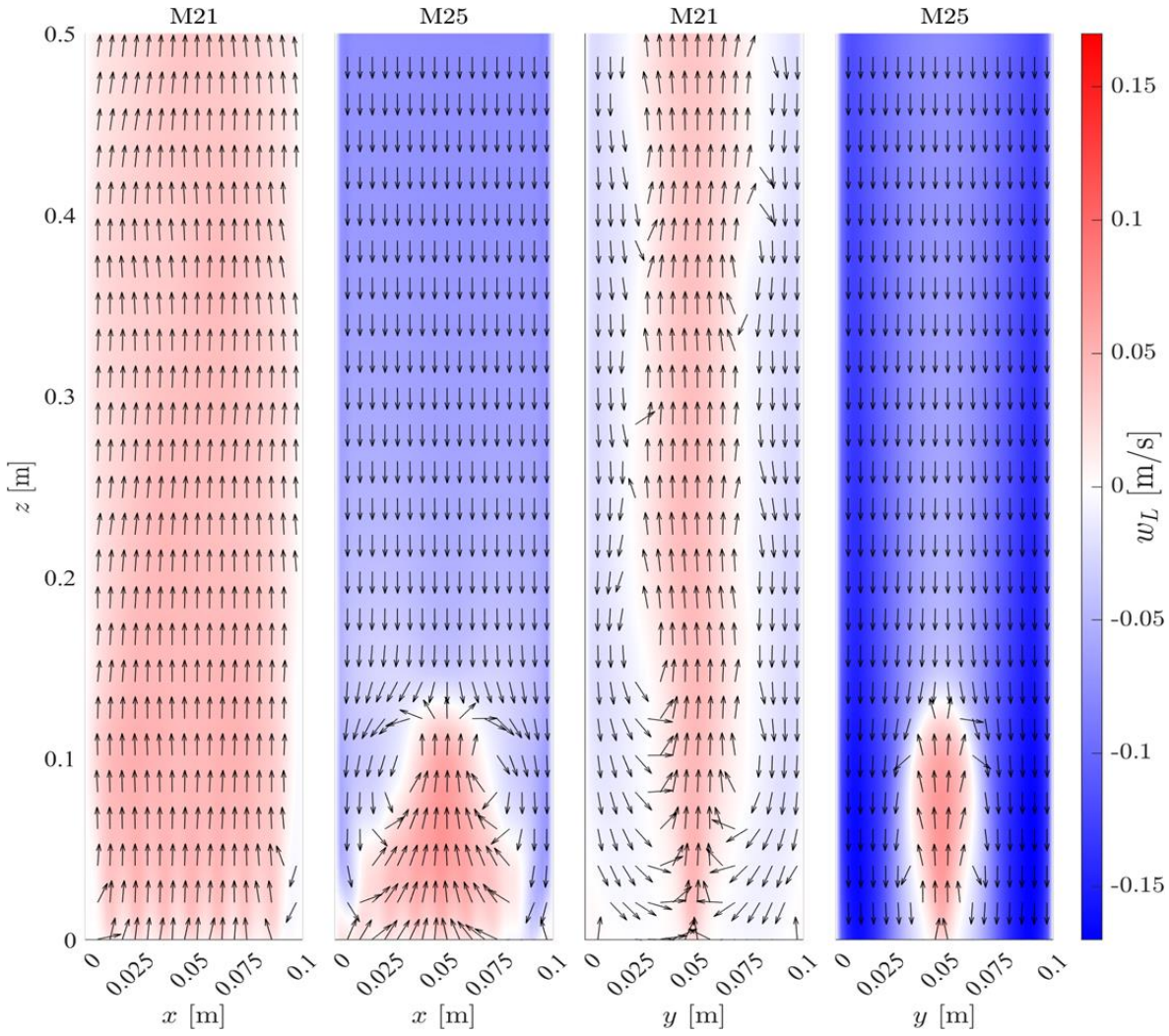

Figure 8: Two-dimensional plots of calculated liquid velocity w_L for cases M21 with low liquid flow rate, Re = 100 and M25 with high liquid flow rate, Re = 9000 as indicated on each panel. Data are shown only up to a height of z = 0.5 m since no further change is observed above. Left two panels x-z plane at $y = D/2$ i.e. showing the column width from left to right along the nozzles, corresponding to the measurement plane; Right two panels y-z plane at $x = D/2$, i.e. showing the column depth from front to back perpendicular to the line of nozzles in the center of the column. Direction of the velocity in the displayed plane is indicated by the arrows, value of its vertical component is color-coded (red indicating upward, blue downward, and white quiescent flow).

Finally, all observables, gas fraction, gas together with relative velocity and liquid velocity at a height of z = 0.5 m are shown in in Figure 9 for both cases comparing the presently adopted lift force model of Hessenkemper et al. (2021) to the earlier one from Tomiyama et al. (2002).

As may be seen, the differences between both models are only minor for the present conditions, both showing good agreement with the measurements for gas fraction and gas velocity but similarly big differences to the liquid velocity measurements.

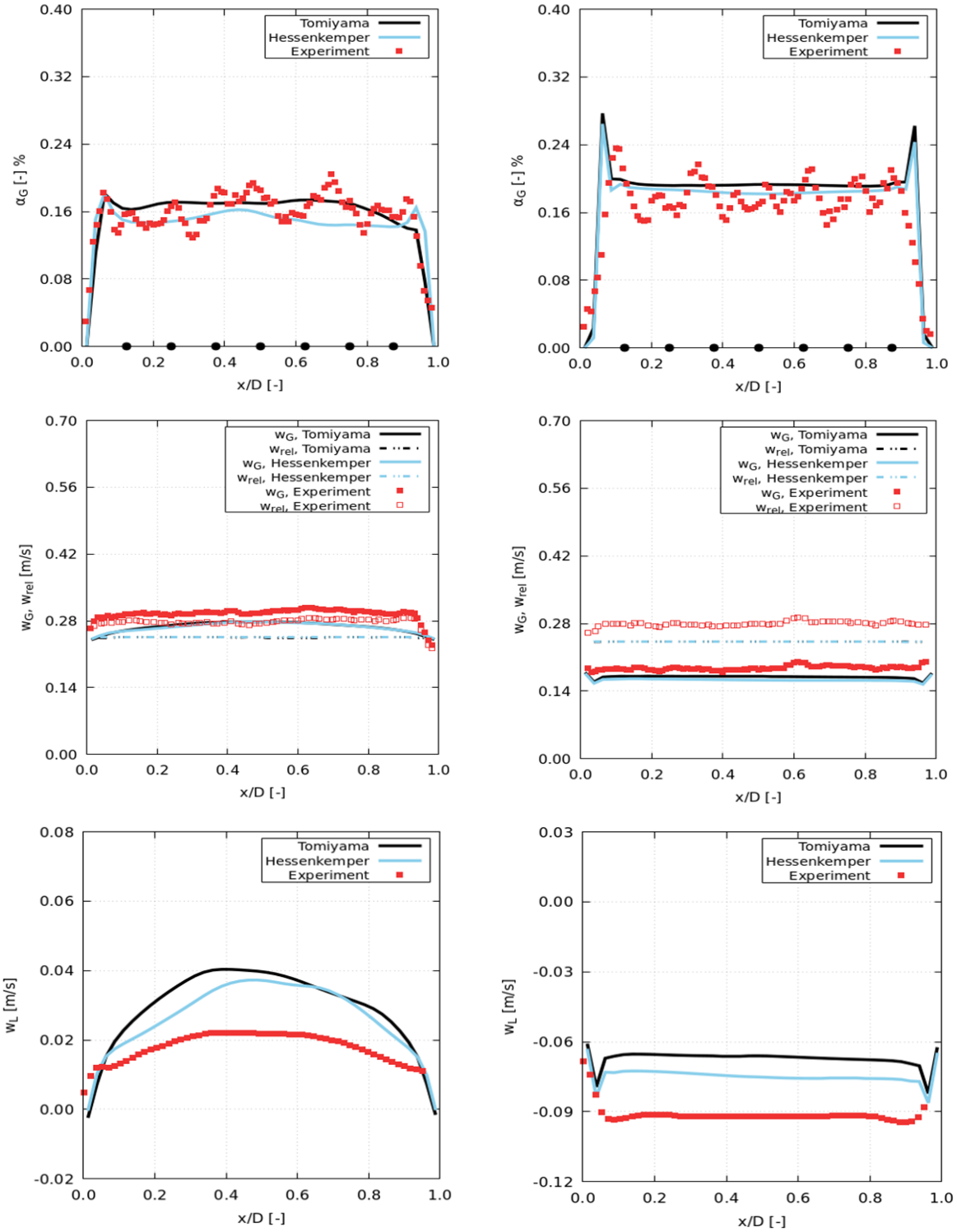

Figure 9: Comparison of measured (symbols) and calculated (lines) results using different drag correlations as indicated in the legends for cases M21 (left column) and M25 (right column) at a height of z = 0.5 m. Top: gas fraction α_G; center: axial gas velocity w_G and relative velocity $w_{rel;}$ bottom: axial liquid velocity w_L.

4.3 Sign change of the lift coefficient

To complete the first brief overview of the database, cases L21 and L25 with the large nozzles are considered, where the mean bubble size in both cases is d_B = 6.4 mm. It is generally acknowledged that for air bubbles in water of this size range, the lift force on the bubbles acts in the direction away from the wall rather than towards it (e.g. Tomiyama et al. 2002, Lucas and Tomiyama 2011, Hessenkemper et al. 2021). As before, only the slightly contaminated drag law from Tomiyama et al. (1998) is considered, but the two models for the lift coefficient from Hessenkemper et al. (2021), Eq. (8), and Tomiyama et al. (2002), Eq. (6), are compared also in the region of negative lift coefficient.

Comparing the results shown for cases L21 and L25 in Figure 10 and Figure 11 with those for cases M21 and M25 of the previous section, it is seen that the gas fraction profiles for both cases have a more rounded shape, with a rather gradual increase from the column walls towards the center and a narrower central region over which they are approximately constant. A similarly more rounded shape is also found for the gas and liquid velocity profiles. This is an obvious manifestation of the opposite direction of the lift force in both sets of cases. Quantitatively, the gas fraction is by ~25% too high in the simulations compared to the experiments. The relative velocity is matched very well for both cases. For the gas velocity a very good match is found in the center of the column, while near the wall it is slightly underpredicted by the simulations. The overprediction of the liquid velocity in the simulations is greatly reduced. In the column center it is only about 15% for the lower liquid flow rate (case L21), while good agreement is found for the higher liquid flow rate (case L25). Near the column walls the simulated liquid velocity is now somewhat lower than the measured one.

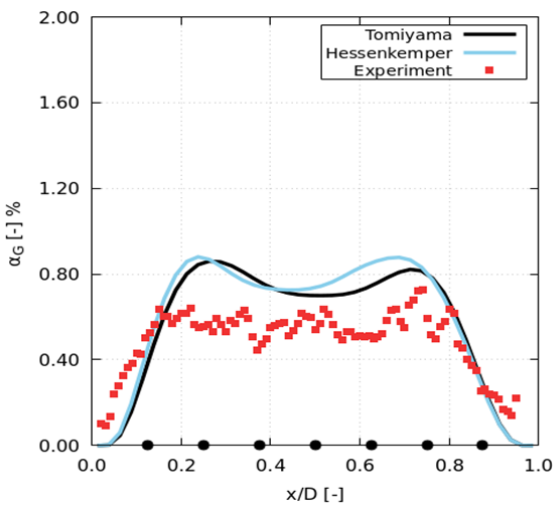

Figure 10: Comparison of measured (symbols) and calculated (lines) results for case L21 at a height of z = 0.5 m. Top left: gas fraction α_G; bottom left: axial gas velocity w_G and relative velocity $w_{rel;}$ bottom right: axial liquid velocity w_L.

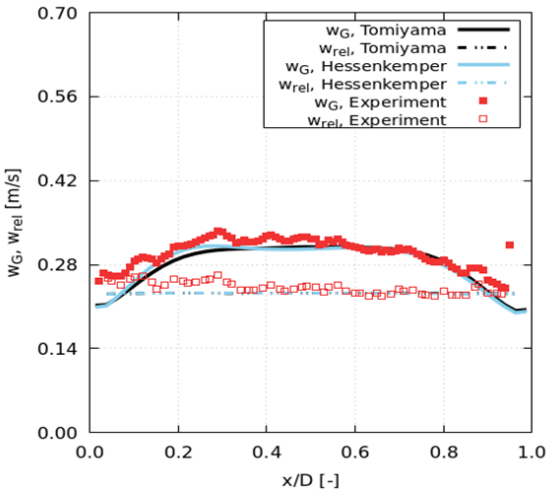

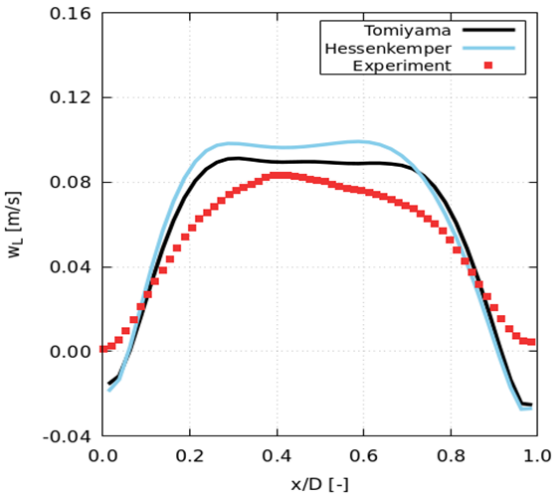

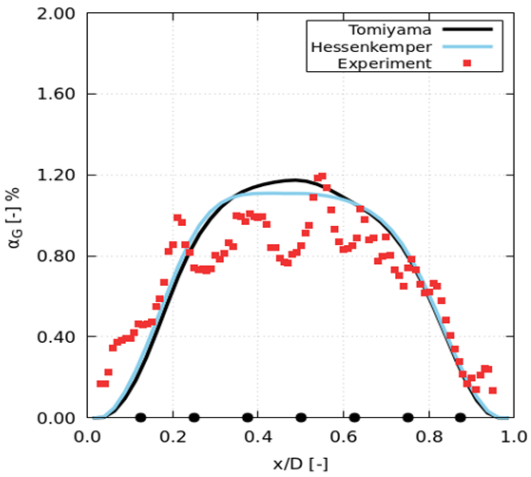

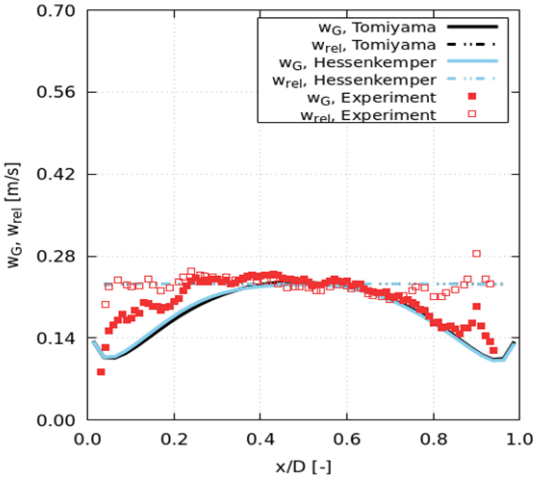

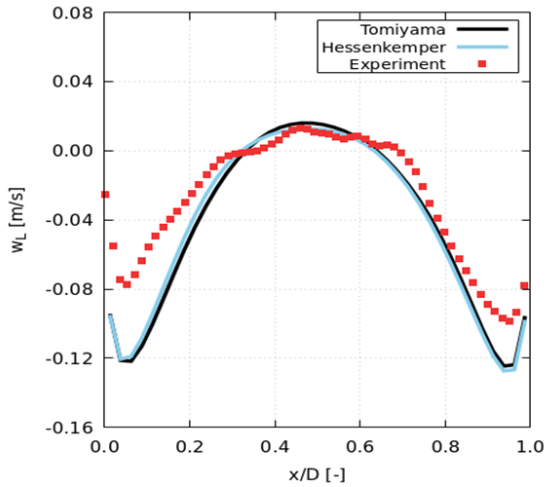

Figure 11: Comparison of measured (symbols) and calculated (lines) results for case L25 at a height of z = 0.5 m. Top left: gas fraction α_G; bottom left: axial gas velocity w_G and relative velocity $w_{rel;}$ bottom right: axial liquid velocity w_L.

Comparing the simulations based on the newer model from Hessenkemper et al. (2021) and the older one from Tomiyama et al. (2002), the influence is found much smaller than the deviations from the experimental data. Hence in this regime of bubble sizes, either lift force correlation could be used.

5 SUMMARY AND CONCLUSIONS

In this combined experimental and numerical investigation of an air-water bubble column with countercurrent flow, gas fractions, bubble and liquid velocities have been acquired, by shadowgraphy, PTV and PIV, and numerically calculated by an Euler-Euler approach. From the large experimental database, six characteristic examples of the comparison between experiment and CFD calculation are presented here, putting an emphasis on different drag law correlations used in the calculations, the comparison of the flow structure and the sign change of the lift force for bigger bubbles.

Concerning the applied models, water quality has long been known to have a strong impact on the drag force experienced by the bubbles and hence on their rise velocity. The present comparison of several different drag models proposed for differing water quality shows good agreement with the measured relative velocities for the slightly contaminated model from Tomiyama et al. (1998). For the lift force, a correlation due to Tomiyama et al. (2002), which was based on mixtures of water and glycerol, has been commonly applied in previous works. This was compared with a new model from Hessenkemper et al. (2021) derived from experiments of air bubbles in water. The latter is closer to the present experimental conditions and hence preferred, although the differences were found to be only minor. For both models, the behavior observed for the small- and medium-nozzle cases, where the lift force acts to push the bubbles towards the column walls, and the large-nozzle cases, where it is directed towards the column center, is very different.

For the cases with smaller bubbles of $d_B \lesssim 5$ mm, it appears, that the main shortcoming of the presently available simulation models is an overprediction of the liquid velocity in the measurement plane, which, due to the three-dimensional structure of the flow, is intimately coupled with the gas distribution, that is highly non-uniform especially along the column depth. A likely reason for the overpredicted liquid velocities is thus that the gas distribution perpendicular to the measurement plane is too strongly peaked in the simulations (note that the reported values represent an average over about one third of the column depth). However, in these cases the liquid velocity is an order of magnitude smaller than the relative velocity and hence its effect on the gas phase is rather small. Since the relative velocity is quite well predicted by the drag force correlation for slightly contaminated bubbles, good agreement is consequently also obtained for the gas velocity and gas fraction in the measurement plane.

For the cases with large bubbles of $d_B \gtrsim 5$ mm, in contrast, the liquid velocity is only mildly overpredicted in the simulations in the column center and even underpredicted near the column walls. Hence, even though it reaches up to about one third of the relative velocity together with the good predictions of the latter a good agreement is also achieved for the gas velocity. The overprediction of the gas fraction in these cases thus is likely a direct consequence of the gas distribution perpendicular to the measurement plane being too strongly peaked in the simulations.

The abundant data, including also bubble parameters like aspect ratio, inclination and velocity direction, and extending further than the six characteristic cases presented here, is currently treated further for the validation and determination of model correlations. The data are available for interested readers through the authors from OVGU Magdeburg.

6 ACKNOWLEDEGEMENT

This work has been carried out in the frame of a joint research project (GZ: RZ 11/3-1 and ZA 527/3-1) funded by the German Research Foundation (DFG).

The authors would also like to acknowledge the help of their students Steffen Erichson and Maximilian Mahler in doing the experiments and parts of the postprocessing. The workshop of LSS is acknowledged for its help in mounting the experimental set-up.

7 NOMENCLATURE

Latin Formula Characters

Symbol	Description	Unit	Symbol	Description	Unit
d_B	mean equivalent sphere diameter	m	p	pressure	Pa
C_D	drag coefficient	-	Q	flow rate	l min^{-1}, l h^{-1}
C_L	lift coefficient	-	Re	column Reynolds number	-
D	column width = depth	m	Re_B	bubble Reynolds number	-
D_H	hydraulic column diameter	m	t	time	s
Eo	Eotvos number	-	$\mathbf{T}$	stress tensor	N m^{-2}
$\boldsymbol{F}$	force per unit volume	N m^{-3}	$\boldsymbol{u}$	velocity	m s^{-1}
$\boldsymbol{g}$	acceleration of gravity	m s^{-2}	w	vertical velocity	m s^{-1}
H	column height	m	x	column width coordinate	m
J	volume flux = superficial velocity	m s^{-1}	y	column depth coordinate	m
k	specific turbulent kinetic energy	m^2 s^{-2}	z	column height coordinate	m

Greek Formula Characters

Symbol	Description	Unit	Symbol	Description	Unit
α	phase fraction	-	ρ	density	kg m^{-3}
ϵ	turbulent dissipation rate	m^2 s^{-3}	σ	surface tension	N m^{-1}
μ	dynamic viscosity	kg m^{-1} s^{-1}	ω	turbulent frequency	s^{-1}
ν	kinematic viscosity	m^2 s^{-1}	$\boldsymbol{\omega}$	vorticity	s^{-1}

Indices

Symbol	Description	Symbol	Description
B	bubble	L	liquid phase
eff	effective	mol	molecular
G	gas phase	rel	relative
$inter$	interface	$turb$	turbulent

8 REFERENCES

Azizi, S., Yadav, A., Lau, Y. M., Hampel, U., Roy, S. and Schubert, M. , 2017 On the experimental investigation of gas-liquid flow in bubble columns using ultrafast X-ray tomography and radioactive particle tracking. *Chemical Engineering Science* 170, 320–331.

Besagni, G., 2021. Bubble column fluid dynamics: A novel perspective for flow regimes and comprehensive experimental investigations. *International Journal of Multiphase Flow*. 135, 103510.

Besagni, G., Guedon, G. R. and Inzoli, F., 2018. Computational fluid-dynamic modeling of the mono-dispersed homogeneous flow regime in bubble columns. *Nuclear Engineering and Design* 331, 222–237.

Besagni, G., Brazzale, P., Fiocca, A. and Inzoli, F., 2016. Estimation of bubble size distributions and shapes in two-phase bubble column using image analysis and optical probes. *Flow Measurement and Instrumentation* 52, 190–207.

Burns, A. D., Frank, T., Hamill, I. and, Shi, J.-M., 2004. The Favre averaged drag model for turbulence dispersion in Eulerian multi-phase flows. *5th International Conference on Multiphase Flow*, ICMF2004, Yokohama, Japan.

Colin, C., Fabre, J. and Kamp, A., 2012. Turbulent bubbly flow in pipe under gravity and microgravity conditions. *Journal of Fluid Mechanics* 711, 469–515.

Colombo, M., Rzehak, R., Fairweather, M., Liao, Y. and Lucas, D., 2021. Benchmarking of computational fluid dynamic models for bubbly flows. *Nuclear Engineering and Design* 375, 111075.

Drew, D. A. and Passman, S. L., 1998. Theory of Multicomponent Fluids, *Springer*.

Fleck, S. and Rzehak, R. Investigation of bubble plume oscillations by Euler-Euler simulation *Chemical Engineering Science*, 2019, 207, 853–861.

Hessenkemper, H., Ziegenhein, T., Rzehak, R., Lucas, D., and Tomiyama, A., 2021. Lift force coefficient of ellipsoidal single bubbles in water. *International Journal of Multiphase Flow* 138, 103587.

Hlawitschka, M. W., Kováts, P., Zähringer, K. and Bart, H. J., 2017. Simulation and experimental validation of reactive bubble column reactors. *Chemical Engineering Science* 170, 306–319.

Hosokawa, S., Tomiyama, A., Misaki, S. and Hamada, T., 2002. Lateral migration of single bubbles due to the presence of wall. *ASME Joint U.S.-European Fluids Engineering Division Conference,* FEDSM2002*,* Montreal, Canada.

Ishii, M. and Hibiki, T., 2011. Thermo-fluid dynamics of two-phase flow. *Springer*, 2nd ed.

Ishii, M. and Zuber, N., 1979. Drag coefficient and relative velocity in bubbly, droplet or particulate flows. *AIChE Journal* 25, 843–855.

Joshi, J. and Nandakumar, K., 2015. Computational modeling of multiphase reactors. *Annual Review of Chemical and Biomolecular Engineering* 6, 347–378.

Khan, H., Lehnigk, R. and Rzehak, R., 2023. Euler-Euler simulation of absorption and desorption in co- and counter-current bubble column flows. *Chemical Engineering Science* 267, 118313.

Kováts, P., Thévenin, D., and Zähringer, K., 2018. Characterizing fluid dynamics in a bubble column aimed for the determination of reactive mass transfer. *Heat and Mass Transfer* 54, 453–461.

Kováts, P., Thévenin, D. and Zähringer, K., 2020. Influence of viscosity and surface tension on bubble dynamics and mass transfer in a model bubble column. *International Journal of Multiphase Flow* 123, 103174.

Kraume, M. 2012. Transportvorgänge in der Verfahrenstechnik. Springer, 2nd ed.

Krepper, E.; Lucas, D. and Rzehak, R., 2016. CFD modelling of downward two phase pipe flow. *9th International Conference on Multiphase Flow*, ICMF2016, Firenze, Italy.

Laleh, A. P., Svrcek, W. Y. and Monnery, W. D., 2012. Design and CFD studies of multiphase separators - a review. *Canadian Journal of Chemical Engineering* 90, 1547–1561.

Liao, J., Ziegenhein, T., and Rzehak, R., 2016. Bubbly flow in an airlift column: a CFD study. *Journal of Chemical Technology & Biotechnology* 91, 2904–2915.

Long, S., Yang, X., Yang, J. and Sommerfeld, M., 2022,. Euler/Euler large eddy simulation of bubbly flow in bubble columns under CO2 chemisorption conditions. *Chemical Engineering Journal* 445, 136654.

Lucas, D., and Tomiyama, A., 2011. On the role of the lateral lift force in poly-dispersed bubbly flows. *International Journal of Multiphase Flow* 37, 1178–1190.

Lucas, D. and Ziegenhein, T., 2019. Influence of the bubble size distribution on the bubble column flow regime. *International Journal of Multiphase Flow* 120, 103092.

Ma, T., Santarelli, C., Ziegenhein, T., Lucas, D., and Froehlich, J., 2017. Direct numerical simulation-based Reynolds-averaged closure for bubble-induced turbulence. *Physical Review Fluids* 2, 034301.

Menter, F. R., 2009. Review of the shear-stress transport turbulence model experience from an industrial perspective. *International Journal of Computational Fluid Dynamics* 23, 305–316.

Mühlbauer, A., Hlawitschka, M. W. and Bart, H. J., 2019. Models for the numerical simulation of bubble columns: A review. *Chemical Engineering & Technology* 91, 1747–1765.

OpenFOAM Foundation, 2022. OpenFOAM v10 User Guide, OpenFOAM Foundation, https://cfd.direct/openfoam/user-guide.

Rzehak, R. and Krepper, E., 2015. Bubbly flows with fixed polydispersity: Validation of a baseline closure model. *Nuclear Engineering and Design* 287, 108–118.

Rzehak, R. and Kriebitzsch, S., 2015. Multiphase CFD-simulation of bubbly pipe flow: A code comparison. *International Journal of Multiphase Flow* 68, 135–152.

Rzehak, R., Krepper, E., Liao, Y., Ziegenhein, T., Kriebitzsch, S., and Lucas, D., 2015. Baseline model for the simulation of bubbly flows. *Chemical Engineering and Technology* 38, 1972–1978.

Rzehak, R., Ziegenhein, T., Kriebitzsch, S., Krepper, E., and Lucas, D., 2017. Unified modeling of bubbly flows in pipes, bubble columns, and airlift columns. *Chemical Engineeing Science* 157, 147–158.

Rzehak, R., Krauß, M., Kovats, P., and Zähringer, K., 2017a. Fluid dynamics in a bubble column: New experiments and simulations. *International Journal of Multiphase Flow* 89, 299–312.

Sathe, M., Joshi, J. and Evans, G., 2013. Characterization of turbulence in rectangular bubble column. *Chemical Engineering Science* 100, 52–68.

Schlegel, F., Bilde, K. G., Draw, M., Evdokimov, I., Hänsch, S., Kamble, V. V., Khan, H., Krull, B., Lehnigk, R., Li, J., Lyu, H., Meller, R., Petelin, G., Kota, S. P., Tekavcic, M.. 2023. HZDR Multiphase Addon for OpenFOAM (Version 10-s.1-hzdr.3). Rodare. http://doi.org/10.14278/rodare.2185.

Shah, Y. T., Kelkar, B. G., Godbole, S. P. and Deckwer, W.-D., 1982. Design parameters estimations for bubble column reactors. *AIChE Journal* 28, 353–379.

Shi, P. and Rzehak, R., 2018. Bubbly flow in stirred tanks: Euler-Euler / RANS modeling. *Chemical Engineering Science* 190, 419–435.

Shi, P., Rzehak, R., Lucas, D. and Magnaudet, J., 2020. Hydrodynamic forces on a clean spherical bubble translating in a wall-bounded linear shear flow. *Physical Review Fluids* 5, 073601.

Schlüter, M., Bothe, D., Herres-Pawlis, S. and Nieken, U., 2021. Reactive Bubbly Flows. *Springer*.

Tomiyama, A., Kataoka, I., Zun, I., and Sakaguchi, T., 1998. Drag coefficients of single bubbles under normal and micro gravity conditions. *JSME International Journal B* 41, 472–479.

Tomiyama, A., Tamai, H., Zun, I., and Hosokawa, S., 2002. Transverse migration of single bubbles in simple shear flows. *Chemical Engineering Science* 57, 1849–1858.

Tyagi, P. and Buwa, V. V., 2017. Experimental characterization of dense gas-liquid flow in a bubble column using voidage probes. *Chemical Engineering Journal* 308, 912–928.

Wanke, D., Silva, B. L., Silva, M. K., Decker, R. K., Utzig, J., Wiggers, V. R. and Meier, H. F., 2015. Turbulence analysis of a cylindrical bubble column. Engineering Sciences and Fundamentals 2015 - Core Programming Area at the 2015 *AIChE Annual Meeting*, 1103–1110.

Werner, S., Kaiser, S. C., Kraume, M., and Eibl, D., 2014. Computational fluid dynamics as a modern tool for engineering characterization of bioreactors. *Pharmaceutical Bioprocessing* 2, 85–99.

Wu, B., 2013. Advances in the use of CFD to characterize, design and optimize bioenergy systems. *Computers and Electronics in Agriculture* 93, 195–208.

Yeoh, G. H. and Tu, J. Y., 2010. Computational Techniques for Multiphase Flows — Basics and Applications. *Butterworth-Heinemann*.

Zidouni, F., Krepper, E., Rzehak, R., Rabha, S., Schubert, M., and Hampel, U., 2015. Simulation of gas-liquid flow in a helical static mixer. *Chemical Engineering Science* 137, 476–486.

Ziegenhein, T., Rzehak, R., Krepper, E., and Lucas, D., 2013. Numerical simulation of polydispersed flow in bubble-columns with the inhomogeneous multi-size-group model. *Chemie Ingenieur Technik* 85, 1080–1091.

Ziegenhein, T., Rzehak, R., Ma, T., and Lucas, D., 2017. A unified approach for modeling uniform and non-uniform bubbly flows. *Canadian Journal of Chemical Engineering* 95, 170–179.